Morphogenesis of maze-like magnetic domains

Cédric Bathany,[1] Maëlane Le Romancer,[1,2] Jason N. Armstrong,[1] and Harsh Deep Chopra[1,*]
[1]*Laboratory for Quantum Devices, Materials Program, Mechanical and Aerospace Engineering Department, State University of New York at Buffalo, Buffalo, New York 14260, USA*
[2]*Département Science des Matériaux, Ecole Polytechnique, Université de Nantes, 44306 Nantes Cedex 03, France*
(Received 3 May 2010; revised manuscript received 20 July 2010; published 9 November 2010)

The present study explains the morphogenesis of maze-like magnetic domains in amorphous Tb-Fe films. It is shown that the observed morphological complexity of the maze-like patterns (which arise due to out-of-plane anisotropy) is superficial and can be explained by simple geometrical rules based on magnetostatic interactions between domains. Morphogenesis in applied field occurs in a fractal-like manner through growth of self-similar reversed domains of various shapes at progressively smaller length scales; the field-dependent fractal dimensions are quantified. The microscopic changes in domain morphology manifest as distinct kinks or "knees" in the macroscopic magnetization curves. Highly aligned synthetic patterns can be formed in microfabricated films, illustrating the potential for "domain engineering" for controlled magnetoelastic response.

DOI: 10.1103/PhysRevB.82.184411 PACS number(s): 75.50.Kj, 75.60.Ch

I. INTRODUCTION

The crystallinity of magnetic materials plays a key role in the observed morphology of domain patterns. In conventional crystals, magnetization spontaneously points along certain preferred directions (the so-called magnetocrystalline anisotropy axes) and individual domains are separated by low-energy domain walls that lie along well-defined crystallographic planes. For example, in iron single crystals, the magnetic easy axis points along the ⟨100⟩-type directions (edges of the cubic unit cell). Therefore, if magnetization in adjacent domains of an iron crystal points along the [100] and [$\bar{1}$00] directions, the low-energy 180° domain wall separating them is parallel to the (010) crystallographic plane. The next level of complexity emerges in multiferroic materials, where the dependence of observed domain morphology on the underlying crystalline medium becomes even more prominent. In multiferroic materials, the formation of ferroelastic twins gives rise to a mosaic of magnetic domains whose geometry is governed by the organization of crystalline tiles (twins) that are oriented in different directions relative to each other.[1,2] The dependence of domain morphology on the crystalline host medium is not only limited to ferromagnets. A similar dependence can be found for domains in antiferromagnets that are internally twinned as a result of phase transition from paramagnetism to antiferromagnetism below the Néel temperature.[3]

Next, consider an amorphous Tb-Fe film with perpendicular anisotropy. In this case, the observed domains form meandering, maze-like patterns of remarkable complexity[4–8] as a result of out-of-plane anisotropy. The stark differences in domain morphology are illustrated in Figs. 1(a)–1(d). Figure 1(a) shows the above-described case for an iron single crystal. Figure 1(b) shows faceted domains on the (001) plane of a twin-free $Co_{50}Ni_{20}Ga_{30}$ single crystal, with magnetization pointing in and out of the plane of the micrograph. Figure 1(c), derived from Ref. 9 for a $Co_{49}Ni_{22}Ga_{29}$ single crystal, shows the domain structure within a set of crystallographic twins running diagonally from bottom left to top right (labeled I, II, I). Each twin contains magnetic domains that are separated by 180°-type walls, and additionally, the twin planes coincide with the 90° walls. In sharp contrast, Fig. 1(d) shows the meandering or sinuous domains in an amorphous Tb-Fe film with perpendicular anisotropy, whose field-dependent morphogenesis is later shown to be self-similar or fractal-like at progressively smaller length scales, and is quantified in the present study.

Note that the formation of labyrinthine domains is not just limited to amorphous film with perpendicular anisotropy. In fact, their morphology share commonality with stripe domains in many ordered systems with perpendicular anisotropy, including garnets, ultrathin films, or sandwiches of Co or Fe, the Fe-Pd and Fe-Pt systems, etc., and their properties

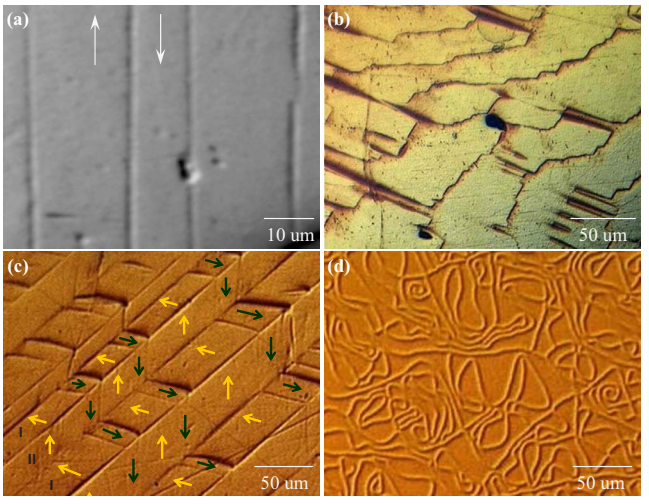

FIG. 1. (Color online) (a) Domain structure in an iron crystal with magnetization vectors along [100] and [$\bar{1}$00] directions in adjacent domains. The 180° domain walls separating them are parallel to the (010) plane. (b) Domain structure in a twin-free $Co_{50}Ni_{20}Ga_{30}$ single crystal at −19 °C. (c) Domain structure in a polytwin of $Co_{49}Ni_{22}Ga_{29}$ single crystal at room temperature, when viewed along the [001] direction. (d) Domain structure in a 2-μm-thick amorphous $Tb_{40}Fe_{60}$ film at 93 °C. The applied field is 1294 Oe and points toward the viewer.

have been well investigated both experimentally and theoretically.[10–19] The domain morphology in Fig. 1(d) also share many similarities with domains in vastly different physical and chemical systems, including type-I superconductors, phospholipids, turing patterns in chemical reaction-diffusion systems, convective roll patterns, confined ferrofluids in magnetic fields, organic systems such as two-dimensional and three-dimensional Langmuir films, etc.; see, for example, an excellent review article in Ref. 20 for a unified treatment of such patterns as arising from modulated phases.

Pertinent to the present system, the point of Fig. 1(d) is to highlight the morphology of magnetic domains in the *absence* of crystallographic planes, and not to discount the formation of labyrinthine domains in other systems. Although the balance of exchange, anisotropy, and magnetostatic energy in the formation of these domains is well understood, the field-dependent morphogenesis of the observed shapes, and geometrical rules underlying their behavior are not so obvious. Moreover, they appear to be complex at first glance. The present study shows that the observed complexity is superficial and the morphology can be explained by simple geometrical rules governed primarily by magnetostatic interactions between domains. Synthetic domain patterns are generated in microfabricated elements with potential for "domain engineering."

II. EXPERIMENTAL DETAILS

The $Tb_{40}Fe_{60}$ films, ranging in thickness from 1 to 2.3 μm were sputter deposited from an alloyed target on Si⟨100⟩ substrates coated with 6 nm Ta seed layer for better adhesion. The sputtering was optimized and carried out at 40 W in an Ar pressure of 2 mTorr in a UHV system whose base pressure was $\sim 10^{-8}$ to 5×10^{-9} Torr. Samples were capped with ~2.5-nm-thick Au protective layer, which was effective in preventing oxidation over time. Transmission electron microscopy (JEOL-2010 high-resolution TEM), scanning electron microscopy (Hitachi SU-70 SEM, 20 kV, 1.0 nm resolution), as well as grazing and wide-angle x-ray diffraction (Rigaku Ultima IV, 40 kV) all confirmed the amorphous nature of the as-deposited films. The magnetization of as-deposited films was normal to the plane of the film. The perpendicular anisotropy is attributed to planar stresses due to substrate constraints, which is known to be sensitive to the argon partial pressure, sputtering power, and film thickness;[21–30] these parameters were carefully optimized. For thickness less than $\sim 0.6-1$ μm, magnetization gradually became in plane due to insufficient buildup of deposition stresses. The magnetization curves were measured by Quantum Design PPMS system with high-temperature vibrating-sample magnetometer (VSM) option, as well as by a room-temperature LakeShore VSM. In-plane and out-of-plane hysteresis curves were measured at various temperatures ranging from 298 to 373 K. The sequence of measurement was from lower to higher temperatures. After high-temperature measurements, hysteresis curves were again measured at room temperature and found to be unchanged.

The magnetic domain structure was studied using the high-resolution interference contrast colloid (ICC) method.[31] The ICC method employs an oil-based colloidal solution to decorate the microfield on a magnetic surface, similar to the versatile Bitter method.[32] However, the technique differs in the manner in which the colloid decorated microfield is detected. In the Bitter method, a problem in contrasts develops in the bright-field or the dark-field mode due to backscattering by particles and various surfaces between the objective lens and the specimen, which results in an overall loss of resolution. Instead, the ICC method uses a Nomarski interferometer to detect the surface microfield distribution. The magnetic microfield on the surface causes local variation in the density of colloid particles (average colloid particle size is 7 nm), thereby delineating the domain structure. This microfield is detected by polarization interferometer optics, which detects any unevenness at the nanometer scale and reveals domain structure with a pronounced three-dimensional effect and at a high-resolution limited only by that of the microscope ($\sim 0.4-0.6$ μm). Other features and capabilities of the ICC method are described elsewhere.[1,33,34] The out-of-plane magnetic field was applied by placing the sample atop the iron core of an electromagnet. The strength of the magnetic field as a function of current was linear and was precalibrated using a Hall probe. For domain imaging, samples were first saturated in either positive or negative field, followed by decrease in field strength to zero and then cycled in the opposite direction. The domain observation system is automated and interfaced with an image frame grabber (Linkam) and a data acquisition card (for applied field and temperature). The experimental setup acquires and labels all images and data automatically. The software operating the acquisition card has the ability to embed important experimental information directly on the recorded optical micrographs, which are automatically collated and numbered as image galleries.

For each micromagnetic experiment, numerous "practice runs" were made to gain facility with the sample response. The strength of the applied field was gradually varied. At the steepest slopes of magnetization curves (where most reversal activity occurs), field strength was changed (increased or decreased) by ~1 Oe (at the rates of ~0.5 Oe/s), followed by observation of domains over periods lasting 1–2 min until no new domain nucleation was detected. At fields with little or no discernable changes in domain patterns, field was varied continuously at the rate of $\sim 1-2$ Oe/s without intermittent pauses. This protocol also enabled the time-dependent formation of reversed domains at a given field to be captured (see, for example, description related to Fig. 4). The domain structure was recorded at the rate of 1 frame per second. The applied field strength was also continuously recorded. The experiments ended with image galleries that can be viewed as movies for later analysis (virtual experiments). The attached movies show selective highlights of the actual experiments.[35] Note that the use of oil-based ferrofluid (instead of water based) is essential for these experiments because of its long-term stability lasting hours to days; water-based ferrofluid simply evaporates after a few minutes (even at room temperature).

III. RESULTS AND DISCUSSION

Hysteresis curves. Whereas films ranging from $1-2.3$ μm thick were deposited, all the following results are

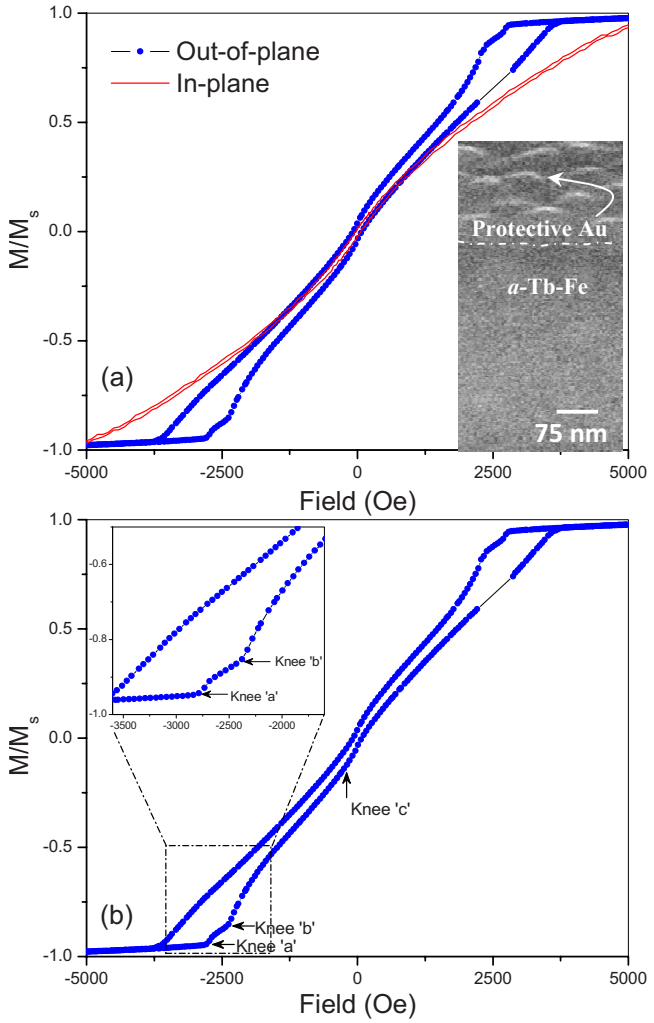

FIG. 2. (Color online) (a) In-plane (red trace) and out-of-plane (blue trace) hysteresis curves for a 2.2-μm-thick amorphous Tb-Fe film at room temperature. Inset shows a high magnification SEM image showing an amorphous film coated with protective gold. (b) Out-of-plane hysteresis curve of the same film marking the position of the three knees, labeled a, b, and c. Inset is a magnified view of knees a and b.

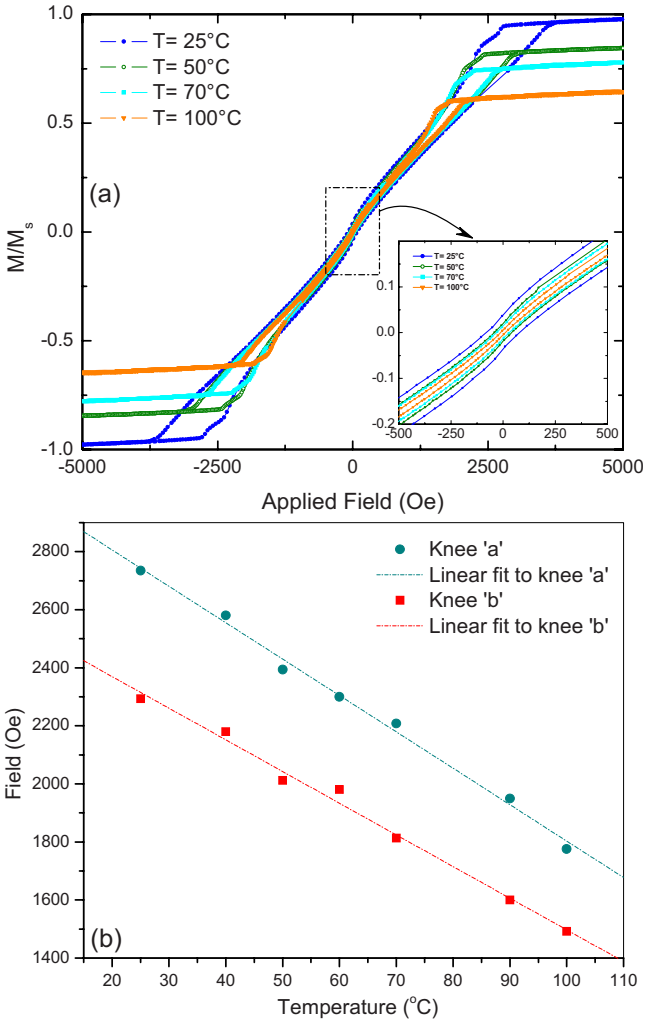

FIG. 3. (Color online) Out-of-plane hysteresis curves for the 2.2-μm-thick amorphous Tb-Fe film at various temperatures. All curves are normalized relative to the trace at 25 °C. Inset shows the zoom-in view of coercivity and remanence. (b) Temperature dependence of knees a and b. Dotted lines are linear fit to the data.

for comparable film thickness ~2–2.3 μm (as noted in each figure caption). Figure 2(a) shows the room temperature, in-plane hysteresis curve (red trace) for a 2.2-μm-thick Tb-Fe film. At room temperature as well as at all temperatures up to 373 K, the film was found to be magnetically isotropic in the plane of the film with magnetization reversal dominated by rotation. The inset in Fig. 2(a) shows a high magnification SEM micrograph (Hitachi SU-70, 1.0 nm resolution) of an as-deposited film in a region near the film surface. The crystallites of protective Au coating can be seen in this cross-section SEM image. As noted in the previous section, TEM, SEM, grazing, and wide-angle x-ray diffraction consistently confirmed the amorphous nature of the films. In contrast to the in-plane magnetization curve, out-of-plane hysteresis curves show peculiar characteristics, as shown in Figs. 2(a) and 2(b) for the same film at room temperature (blue trace). At first sight, the skewed out-of-plane hysteresis curve also appears to be dominated by rotation in its approach to saturation. However, notice the uncharacteristically large hysteresis near saturation fields. By comparison, the hysteresis is minimal at low fields. Curves with similar characteristics (i.e., narrow at low fields and broad at high fields) have been previously observed in Fe-Pd films with perpendicular anisotropy;[14,15,36] Refs. 14 and 15 also include a discussion for deriving various useful parameters, including domain periodicity. In addition, well-defined stripe domain patterns could be engineered using focused ion-beam irradiation.[15]

A closer examination of the curve in Fig. 2(b) reveals the presence of two kinks or knees at high fields (labeled "a" and "b") along with a third softer knee (labeled "c") that appears just before remanence; such knees have not been discussed or noted in previous studies. The inset in Fig. 2(b) is a zoom-in view of knees a and b. Figure 3(a) shows out-of-plane hysteresis curves for the film at various temperatures. As expected, higher temperatures shrink the hysteresis curves toward lower saturation values. Whereas at 298 K the sample reaches saturation at ~3700 Oe, at 373 K saturation is achieved at ~2100 Oe. In addition, the inset in Fig. 3(a)

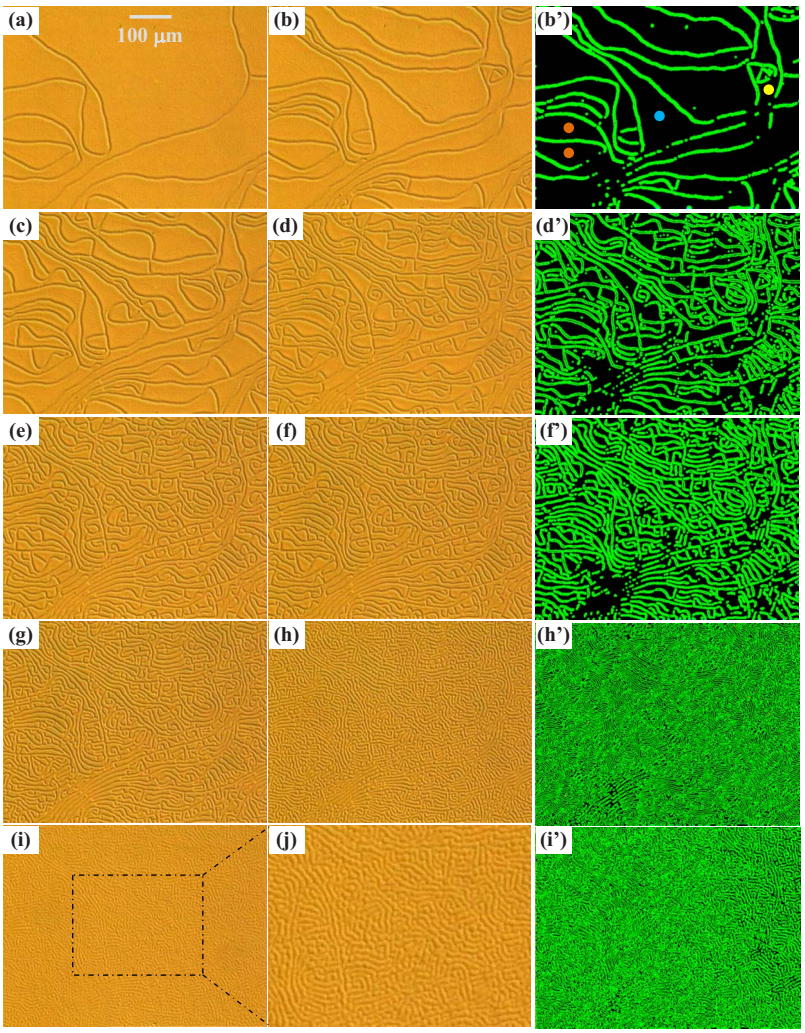

FIG. 4. (Color online) [(a)–(i)] Micrographs showing the evolution of domain structure versus field in the 2.2-μm-thick amorphous Tb-Fe film at ~100 °C as the field is reduced from negative saturation to zero. (j) Zoom-in view of the domain structure corresponding to the area inscribed within the rectangle in (i). Pictures in (b′), (d′), (f′), (h′), and (i′) are schematic renderings of the micrographs in (b), (d), (f), (h), and (i), respectively, which highlights progressive subdivision of unreversed (black) domains demarcated by reversed domains (green). The schematic renderings can be obtained by an edge-finding routine of image-analysis software. Applied fields are (a) −1800 Oe, (b) −1200 Oe, (c) −1200 Oe, (d) −1100 Oe, (e) −1000 Oe, (f) −1000 Oe, (g) −850 Oe, (h) −600 Oe, and (i) −200 Oe. See text for further explanation.

shows that both remanence and coercivity becomes smaller at higher temperatures. Figure 3(b) plots the temperature dependence of knees a and b, both of which exhibits a linear downward shift with increasing temperature. It was difficult to reasonably approximate the temperature dependence of the soft knee c but its relevance along with those of knees a and b is discussed with reference to the observed field-dependent micromagnetic (domain) structure in the following.

Micromagnetic structure in films. The micromagnetic structure was investigated at various temperatures and Fig. 4 describes its salient features using the example of magnetization reversal for the above film at ~373 K (100 °C). In all the following figures and discussion, the direction of applied field is normal to the plane of the film (either pointing outward or inward). The micromagnetic structures in Fig. 4 correspond to the highlighted section of the hysteresis curve shown in Fig. 5. Also note that while only a few representative micrographs can be realistically included in Fig. 4, the attached Movie-1 in the Supplementary Documents shows the reversal process in a more continuous manner and in greater detail.[35] Following saturation in the negative direction, Fig. 4 and Movie-1 shows that demagnetization occurs primarily by nucleation and growth of reversed domains as the field strength is reduced from negative saturation to zero. Notice that without micromagnetic studies one could have misconstrued the slant of the out-of-plane hysteresis curves in Figs. 2 and 3 as arising from a rotation-dominated magnetization reversal process. Instead, as described in the following, the observed slant results from demagnetization by a *self-similar growth process* for the reversed domains within progressively smaller regions, as the sample is brought from

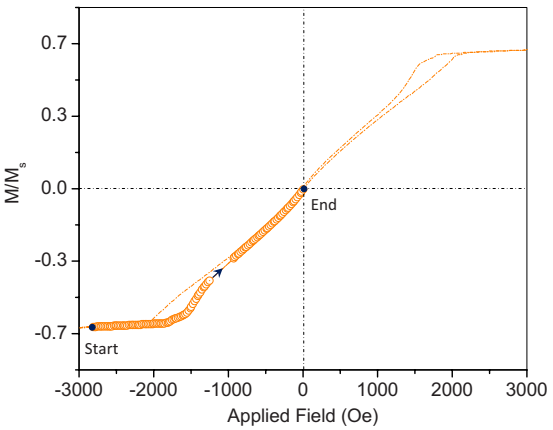

FIG. 5. (Color online) Section of the hysteresis curve corresponding to the micromagnetic structures shown in Fig. 4 (highlighted by the symbols).

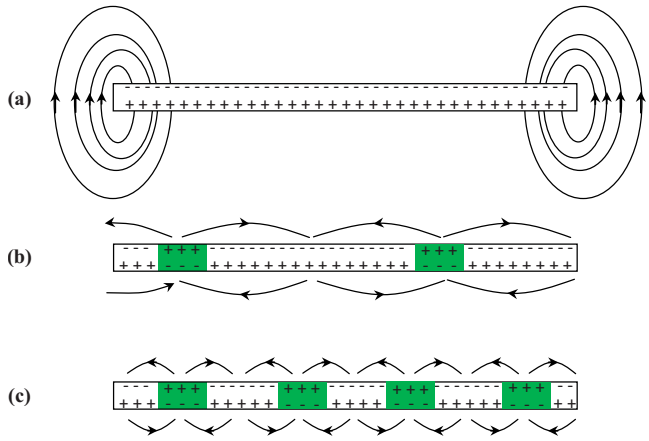

FIG. 6. (Color online) Progressive subdivision of the film into domains to lower the overall magnetostatic energy.

saturation to remanence. Starting from a single-domain state at a negative saturation (not shown in Fig. 4, see Movie-1), reversal begins by abrupt formation of narrow, serpentine-like reversed domains, as shown in Figs. 4(a) and 4(b). The magnetization in the reversed domains points toward the viewer whereas it points directly into the plane of the film in the remaining unreversed regions of the film.

Although the geometrical arrangement of the meandering reversed domains is random and the geometrical patterns vary from one experiment to another, the overall tendency of the reversed domains is to spread across the entire surface of the sample (as opposed to local nucleation of one or few domains and their subsequent growth and penetration into the sample). In this manner, the reversed domains subdivide the initial unreversed single domain at negative saturation into N unreversed cells. Figure 4(b′) is a schematic rendering of the micrograph in Fig. 4(b), which shows several (black) unreversed domains demarcated by reversed domains (green). Following the initial subdivision in Fig. 4(b), further reversal occurs in a self-similar manner by continued subdivision of unreversed regions into progressively smaller cells. Moreover, *within each unreversed cell the reversal occur independent of reversal in adjacent regions*. For example, follow the progressive subdivision of the unreversed domain marked by the (blue) dot in the middle of Fig. 4(b′). New reversed domains can be seen to nucleate as branches from the existing reversed domains. For instance, in Fig. 4(d) or its schematic rendering in Fig. 4(d′), the region marked by the (blue) dot in Fig. 4(b′) is subdivided into smaller regions. This process continues on ever finer length scales, as shown in Figs. 4(e), 4(f), and 4(f′), Figs. 4(g), 4(h), and 4(h′), and Figs. 4(i) and 4(i′); Fig. 4(i) is a zoom-in view of the region marked in Fig. 4(i). Also note the time-dependent formation of reversed domains at constant field values in Movie-1.[35]

The observed tendency of the reversed domains to spread across the entire film surface can be understood in terms of lowering of the overall magnetostatic energy, as shown schematically in Fig. 6. Initially, the single-domain state at (negative) saturation, Fig. 6(a), sets up magnetic poles at the top and bottom surfaces of the film and an associated high-energy density $\sim M_s^2$ that is only stable under sufficiently strong fields. Formation of reversed domains across the entire film surface "magnetically shatters" the single unreversed domain into N unreversed cells, Fig. 6(b), thereby lowering the magnetostatic energy by $\sim 1/N$. Note that the observed energetics of reducing the magnetostatic energy in case of amorphous medium have the same basis as that for crystalline materials.[37] With further subdivision of the unreversed regions into smaller cells, Fig. 6(c), the magnetostatic energy is further reduced. From Fig. 4, notice the effectiveness of this process in uniformly demagnetizing the sample across the entire area of the film as it approaches the state of remanence. *The process does not leave out any obviously large regions of unreversed domains as the field strength is reduced.*

Figure 4 above shows progressive subdivision of the sample into finer domains until the net magnetization is nearly zero at remanence. Flux closure occurs by similarly sized regions of reversed and unreversed domains that are intermingled within close proximity. Now if the field is increased from zero to, say positive saturation, approach to a single-domain state (saturation) is found to be the reverse of that described in Fig. 4. Finer domains locally unreverse themselves to form coarser cells, until ultimately a single-domain state corresponding to saturation is left. This is shown sequentially in Figs. 7(a)–7(h). Again, the attached Movie-2 shows the above-described features in a more continuous manner and in greater detail.[35] For instance, notice the distinct change in average size of reversed cells in Movie-2 corresponding to the micrographs shown in Figs. 7(c)–7(e). Also, for generality, the micrographs in Fig. 7 are shown for a field cycle immediately preceding Fig. 4, that is, the shown figures are from remanence to negative saturation. In sharp comparison to conventional crystalline materials, notice that there is *no lateral displacement* of the reversed domains but only elongation (towards remanence) or shrinkage (toward saturation).

Over repeated experiments, the following observations can be made (elaborated below): (I) *the knee a corresponds to the appearance of the first set of reversed domains that subdivide a single unreversed domain into a multiplicity of unreversed domains.* (II) *Subsequent reversal process in any unreversed region occurs independent of reversal in adjacent regions*.

These observations also explain the broadening of the out-of-plane hysteresis curves in Figs. 1 and 2 near saturation and thinning toward zero field. Also note that while the domain patterns appear to be seemingly random, the guiding principle is self-similar growth of reversed domains, which is highlighted in Figs. 8 and 9 next.

Self-similar growth. The morphogenesis of reversed domains in Figs. 4 and 7 seemingly evolves into complex geometrical patterns. However, a closer examination reveals remarkable simplicity. This is shown in Figs. 8(a)–8(i) using the region defined by the pair of (orange) dots near middle-left in Fig. 4(b′). Each schematic in Figs. 8(a′)–8(i′) is a near exact and idealized trace of the respective micrograph in Figs. 8(a)–8(i). The color scheme in the schematics describes the order of the reversed domain, as shown by the "order tree" at the bottom right of Fig. 8. For example, a domain that nucleates from an existing first-order reversed domain is

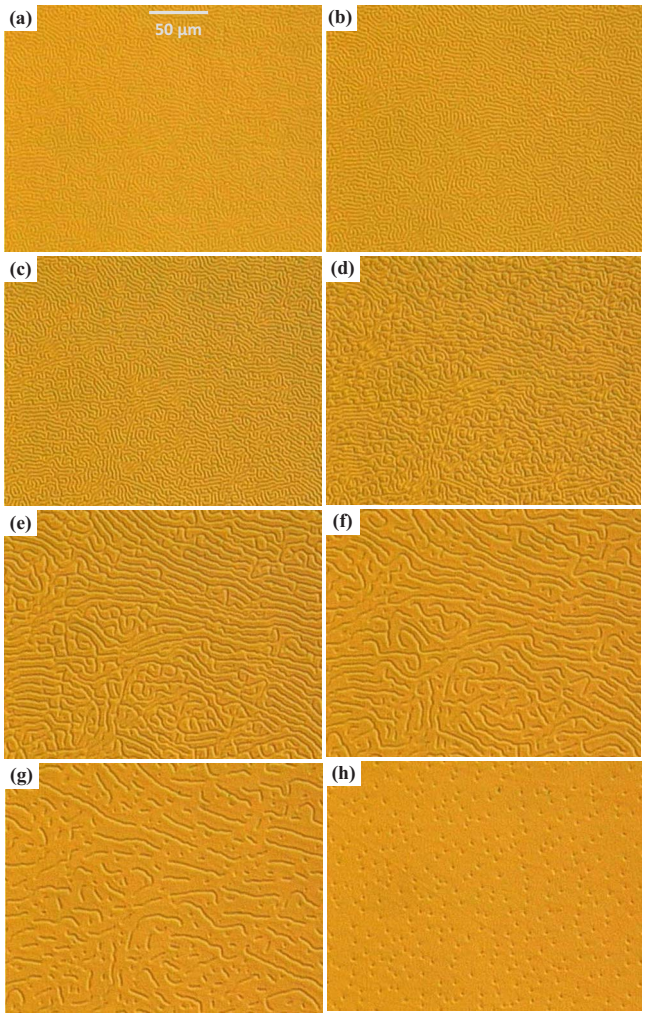

FIG. 7. (Color online) [(a)–(h)] Micrographs showing the evolution of domain structure versus field in the 2.2-μm-thick amorphous Tb-Fe film at ~100 °C as the field is increased from zero to negative saturation. Applied fields are (a) −200 Oe, (b) −400 Oe, (c) −900 Oe, (d) −1200 Oe, (e) −1500 Oe, (f) −1600 Oe, (g) −1600 Oe, and (h) −1600 Oe. The micrographs correspond to the field cycle immediately preceding Fig. 4. See text for further explanation.

traced in green, representing a second-order domain. The zero-order reversed domains in Fig. 8(a′) represent the first set of domains that nucleate following saturation in the negative direction (corresponding to knee a). As shown in Fig. 8(b), two sinuous first-order reversed domains first nucleate on either side of an existing domain at the center (along with formation of domains in the upper-right corner). In the following this undulating shape is referred to as the open form of "Maiandros" (derived from Maiandros or Maeander river in ancient Greek mythology and now often used in reference to such undulating or meandering geometrical forms), and it was the most commonly observed geometrical form; closed forms of Maiandros are shown later. Although terms such as "meandering domains" or "labyrinthine/stripe domains" are commonly used, use of a single noun (Maiandros) is efficient and provides ease of description for open or closed forms; see also Ref. 38. Figure 8 shows that the apparently complex domain patterns are in fact relatively simple and composed of the same open geometrical form that gradually fills in the unreversed regions at progressively smaller scales. Also note that the growth of open Maiandros does not follow a strictly hierarchical sequence as a function of applied field. In other words, lower order reversed domains (e.g., first or second) may still continue to form in different regions while higher order domains (e.g., third and fourth) are being formed; see, for example, Figs. 8(h) and 8(i). Also notice that within the available optical resolution (~0.4 μm) first-, second-, and third-order domains are the most prevalent with only a few instances of fourth-order domains that can only be seen in Figs. 8(h) and 8(h′), 8(i) and 8(i′).

Figure 9 shows an example of a closed form of Maiandros in the shape of the triangle (ignoring the obvious rounding of edges that occurs to avoid sharp magnetization gradients). These micrographs correspond to the region near the (yellow) dot in the upper-right side of Fig. 4(b′). Again, each schematic in Figs. 9(a′)–9(d′) adjacent to each micrograph in Figs. 9(a)–9(d) is a near exact and idealized trace of the respective micrograph. The color scheme in the schematics follows the same order tree shown at the bottom of Fig. 8. Figure 9(e) is a hypothetical schematic of a region undergoing reversal by triangular form of Maiandros alone.

From the above discussion it is clear that the observed *micromagnetic patterns are formed recursively by random propagation of self-similar geometrical forms at progressively smaller regions*. This recursive size reduction at different length scales can also be seen clearly in Movie-3 of the attached Supplementary documents.[35] It corresponds to the sample shown earlier in Fig. 1(d) and it succeeds in capturing the progressive cell division with greater clarity than that shown previously in Movie-1. These patterns can be characterized by fractal geometry, and the fractal dimensions corresponding to the morphogenesis of reversed domains is quantified and enumerated following a discussion of subtle energy differences between various patterns.

Patterns in microfabricated elements. Owning to the large area of the film, different random patterns of zero-order reversed domain emerge in successive experiments; these patterns are then subsequently filled in by higher order domains. By reducing the area of the film using microfabrication, the number of nuclei can be controlled. Use of microfabricated films, where magnetostatic end effects dominate, also yields insight into the subtle energy differences between different domain patterns, which in turn, enable control over their geometrical morphogenesis. Also, given that the apparently complex domain patterns can be described by minimization of the magnetostatic energy, an ability to engineer domain morphology in micro-electro-mechanical system (MEMS) elements (where edge effects are dominant) would provide new means to control the switching characteristics of these films for integration in MEMS devices. Figure 10(a) shows a microfabricated film in the form of a narrow taper. Reversal in this film begins by two nuclei shown encircled in Fig. 10(a). As the field strength is reduced, another nucleus forms toward the left of the tapered film, as shown encircled in Fig. 10(b). This nucleus subsequently grows into an open Maiandros, as shown in Fig. 10(c). With further reduction in applied field, Fig. 10(d) shows the nucleation of several sec-

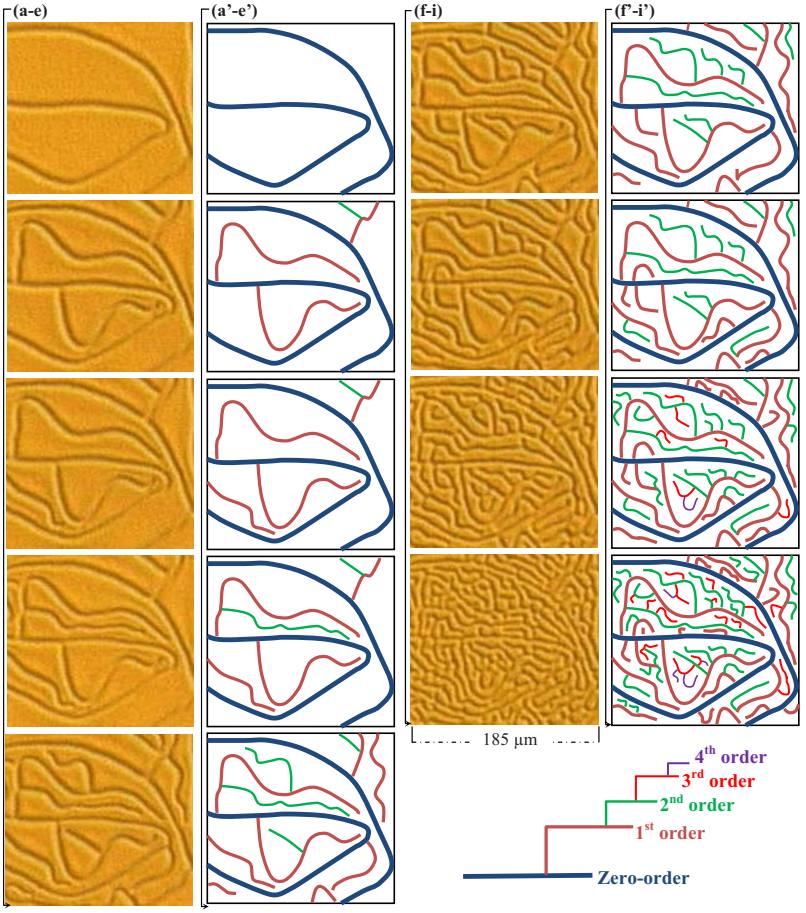

FIG. 8. (Color online) [(a)–(i)] Self-similar growth of reversed domains over progressively smaller areas by open form of Maiandros. The micrographs are zoom-in views of the region marked by two (orange) dots in Fig. 4(b′). [(a′)–(i′)] Near-exact schematic traces of adjacent micrographs in (a)–(i), respectively. The order tree at the bottom right describes the order of reversed domain. See text for explanation. Applied fields are (a) −1800 Oe, (b) −1200 Oe, (c) −1200 Oe, (d) −1000 Oe, (e) −1000 Oe, (f) −1000 Oe, (g) −1000 Oe, (h) −840 Oe, and (i) −600 Oe.

ondary open Maiandros that fill in the unreversed regions of the film. Figure 10(e) shows the nucleation of a new secondary Maiandros toward the tapered end of the film, whose point of nucleation is marked by the vertical arrow. The observed nucleation and growth pattern could be repeated over successive experiments, within small differences. Figure 1(f) shows a subsequent experiment at twice the magnification, showing the same secondary Maiandros marked in Fig. 10(e). Figures 10(g) and 10(h) shows, respectively, the successive growth of two additional Maiandros into the ever narrowing region of the film (marked by arrows), where their shape is rendered into a straight line. *This suggests that the limiting shape of an undulating open Maiandros is a straight line*. The total energy of a straight domain-wall segment is lower than that for a wavy segment (equal to $\sigma \cdot A$; σ is wall energy per unit area and A is the total wall area). To explain, consider the schematic of plane-parallel set of reversed domains in Fig. 11(a). The magnetization in the reversed domains points toward the viewer (●) whereas in unreversed domains it points into the plane of the figure (⊗). As a result, the flux emanating from reversed domains closes its path with adjacent unreversed domains, as shown by the arrows in the lower-left section of Fig. 11(a). From magnetostatic consideration it is clear that repulsive forces between flux of same polarity precludes the intersection of one reversed domain with another and this condition is always experimentally met. In other words, *reversed domains never intersect with each other although they may nucleate as limbs from existing domains*. If existing reversed domains are parallel and sufficiently close to each other, magnetostatic forces of repulsion between them define the midrib between them as locus of new domain growth, as shown in Fig. 11(a). Under such conditions, parallel growth would dominate. However, if the reversed domains are sufficiently far apart and if a new reversed domain nucleates as a limb from an existing domain, its trajectory would be defined by magnetostatic forces of repulsion with existing domain(s) that it approaches, and the locus of the resulting trajectory would be a closed or open form of Maiandros. An example of this is shown in Fig. 11(b). The experimental realization of a plane-parallel assembly of reversed domains under controlled nucleation and growth is discussed below followed by two simple rules for initial trajectory of nuclei and their subsequent growth direction.

Assembly of plane-parallel domains. Figures 12(a)–12(d) shows progressive morphogenesis of reversed domains into a near-perfect plane-parallel assembly, analogous to the schematic shown in Fig. 11(a). The attached Movie-4 shows the reversal in greater detail.[35] Figure 12(a) and Movie-4 shows that reversal begins by formation of numerous nuclei that grow into plane-parallel domains. Nuclei that are interspersed within these plane-parallel domains are forced to grow in the same direction due to repulsive magnetostatic interactions between adjacent domains. Whereas no two resulting patterns are ever the same, globally, a set of plane-parallel reversed domains could be formed over repeated experiments.

Imperfect assembly of plane-parallel domains. Figures

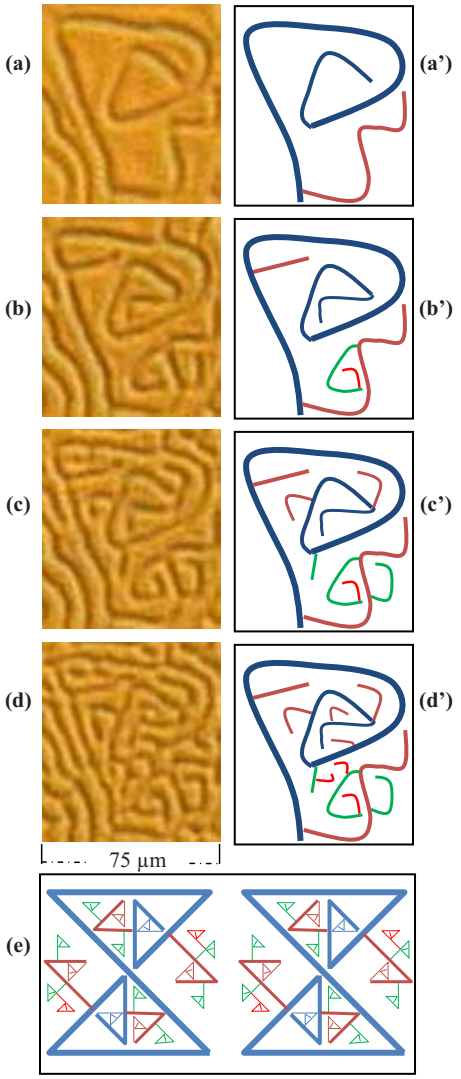

FIG. 9. (Color online) [(a)–(d)] Self-similar growth of reversed domains over progressively smaller areas by closed form of Maiandros. The micrographs are zoom-in views of the region marked by the (yellow) dots in Fig. 4(b′). [(a′)–(d′)] Near-exact schematic traces of adjacent micrographs in (a)–(d), respectively. The order tree is the same as that shown in Fig. 6. See text for explanation. Applied fields are (a) −1200 Oe, (b) −1000 Oe, (c) −840 Oe, and (d) −600 Oe. (e) A hypothetical schematic showing reversal by triangular Maiandros only.

13(a)–13(f) shows progressive morphogenesis of reversed domains in another microfabricated film. The attached Movie-5 corresponds to micrographs in Fig. 13.[35] Figures 13(a)–13(c) and Movie-5 shows that reversal initially begins by nucleation of several domains, followed by their plane-parallel growth. During this process the interspersed reversed nuclei are forced to grow in the same direction. However, with further reduction in applied field, accidental nucleation of domains occurs as branches of horizontal domains, as shown in Fig. 13(d). This causes the subsequent growth morphology to change in order to fill the remaining regions of the film, as shown in Figs. 13(e) and 13(f). For instance, the lower part of the triangular film is split into two new triangular regions in Fig. 13(d), within which new domain primarily grows in the vertical direction, as shown in Figs. 13(e) and 13(f) and Movie-5.

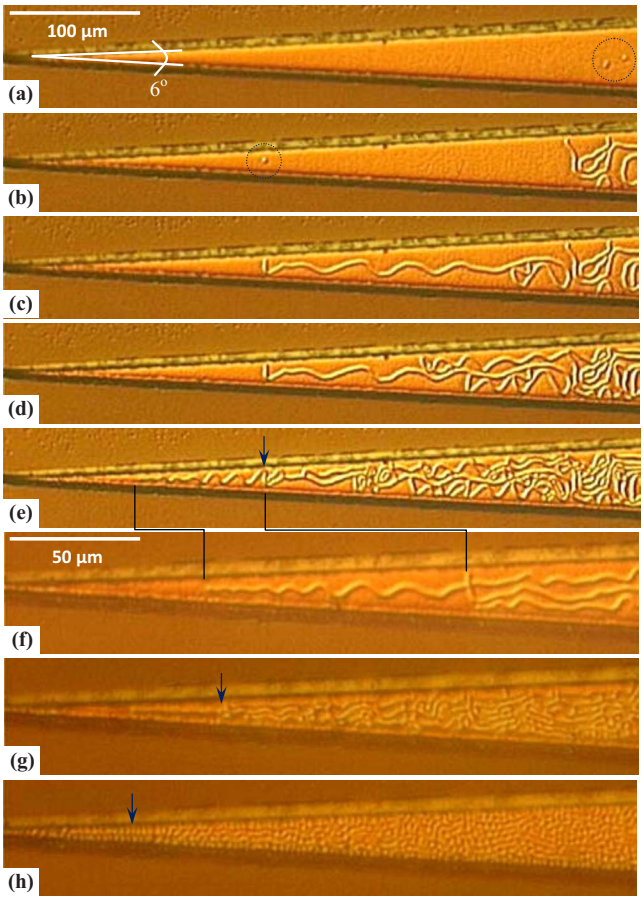

FIG. 10. (Color online) [(a)–(e)] Nucleation and growth of open form of Maiandros in a microfabricated film that is shaped into a narrow taper (included angle is 6°). The film thickness is ~2 μm and temperature is 80.5 °C. [(f)–(h)] Nucleation and growth in the same film during another experiment but at twice the magnification. Notice that the open form of Maiandros takes the limiting shape of a straight line as it penetrates the narrowest regions of the tapered film. Applied fields are (a) 1454 Oe, (b) 1187 Oe, (c) 1158 Oe, (d) 1075 Oe, (e) 1025 Oe, (f) 1038 Oe, (g) 803 Oe, and (h) 276 Oe.

Random Pattern. Figures 14(a)–14(d) shows progressive morphogenesis of reversed domains in the same microfabricated film as in Fig. 13 except that the applied field was slowly decreased until just one or few nuclei became visible. The attached Movie-6 corresponds to micrographs in Fig. 14 and show the reversal in greater detail.[35] In contrast to Figs. 12 and 13, Fig. 14(a) and Movie-6 show that reversal begins by formation of only two nuclei, as shown encircled in Fig. 14(a). Figure 14(b) shows that these two nuclei grow in the horizontal direction and another nucleus forms at the upper-left corner of the film. Figure 14(c) shows that the reversed domains deflect off the edges of the triangle due to magnetostatic forces. Subsequent growth occurs by formation of several new secondary branches of reversed domains. As a result, the entire film is randomly populated with open and closed forms of Maiandros, as shown in Figs. 14(d)–14(f) and Movie-6. Note that although a precise study of nucleation rate as a function of temperature and sweep rate of

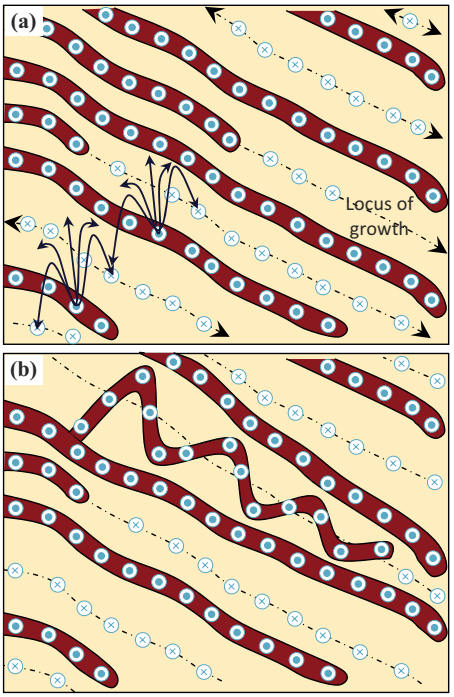

FIG. 11. (Color online) (a) Schematic of plane-parallel set of reversed domains that are sufficiently close to each other. The midrib between them defines the locus of growth for new domains. (b) For reversed domains that are far apart, nucleation of a reversed domain as limb of an existing domain gives rise to meandering domains. See text for explanation.

applied field is beyond the scope of the present study, formation of one or few nuclei could be experimentally achieved by slowly reducing the field in small fractions of an oersted

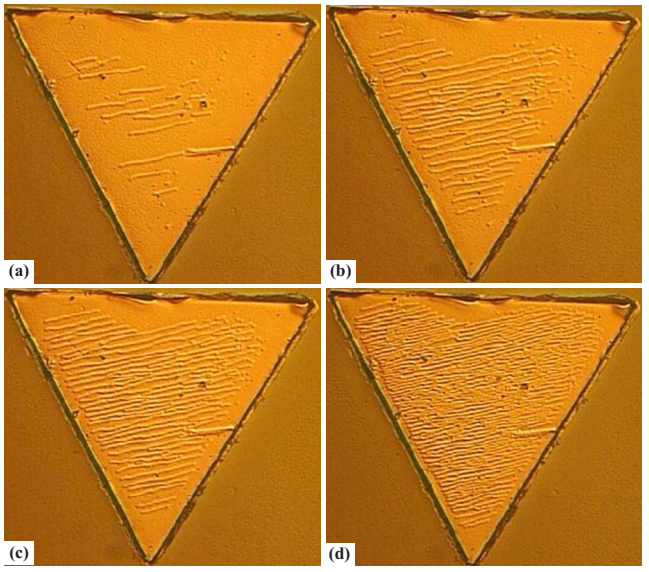

FIG. 12. (Color online) [(a)–(d)] Nucleation and growth of a near-perfect plane-parallel assembly of reversed domains in a microfabricated film in the shape of an equilateral triangle. Applied fields are (a) −1278 Oe, (b) −1238 Oe, (c) −1236 Oe, and (d) −1081 Oe. The film thickness is ~2.3 μm and temperature is 54.5 °C. The edge length of the triangle is 150 μm.

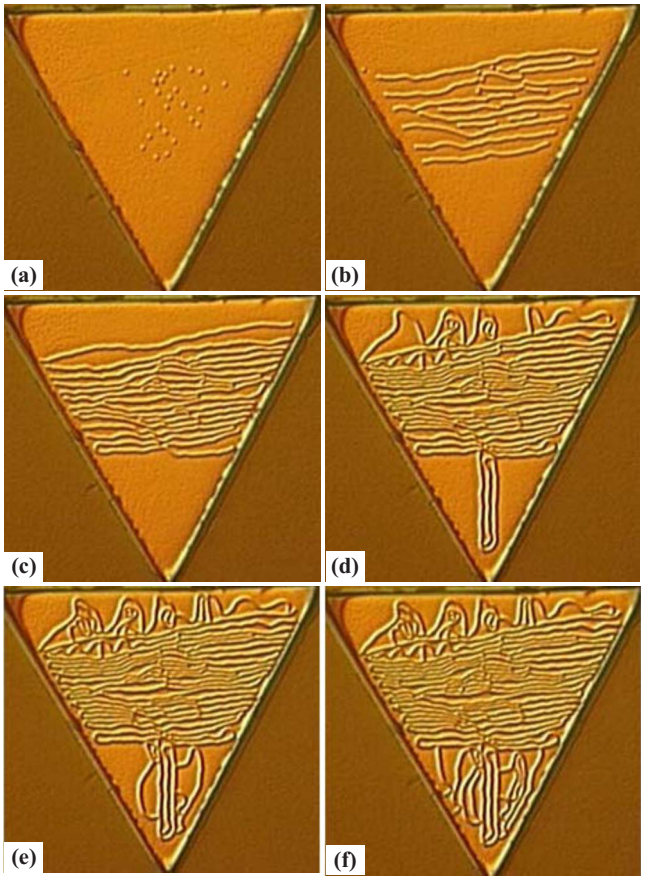

FIG. 13. (Color online) [(a)–(f)] Nucleation and growth of an imperfect assembly of plane-parallel domains within a microfabricated film in the shape of an equilateral triangle. Applied fields are (a) 1316 Oe, (b) 1167 Oe, (c) 1044 Oe, (d) 975 Oe, (e) 960 Oe, and (f) 954 Oe. The film thickness is ~2 μm and temperature is 80.5 °C. The edge length of the triangle is 100 μm.

and holding the sample at that field, followed by a further small decrease in field. In contrast, rapid decrease in field at a given temperature is akin to supercooling, which can result in a large number of nuclei to form suddenly.

Dipolar or magnetostatic forces between flux of same orientation dictates the following two simple rules for the observed forms of reversed domains:

Geometrical rule-1: orthogonality. The initial trajectory of a reversed domain that nucleates as a limb of an existing reversed domain is orthogonal to the existing domain at the point of nucleation.

This is shown schematically in the inset of Fig. 15, along with several encircled examples of this rule in the micrograph shown in Fig. 15. This condition is a natural consequence of the fact that magnetostatic forces (and hence locus of domain growth) are balanced normal to the point of nucleation.

Geometrical rule-2: bisection. The locus of any Maiandros (open or closed) as it approaches another segment of reversed domain is the bisector of the angle between the two. For cases involving more than two domain segments, the superposition principle applies by summing over all interactions.

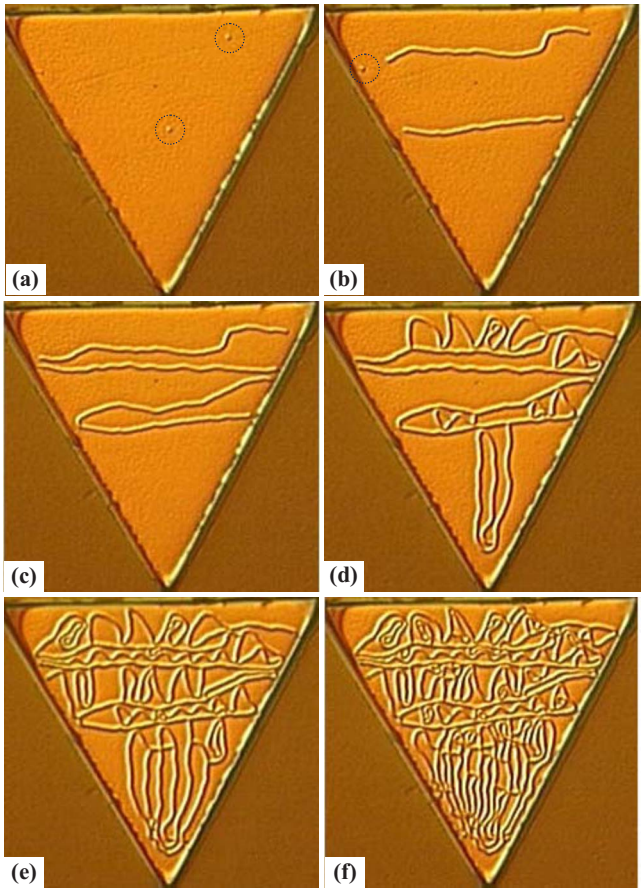

FIG. 14. (Color online) [(a)–(f)] Nucleation and growth of a disordered assembly of plane-parallel domains within a microfabricated film in the shape of an equilateral triangle. Applied fields are (a) 1391 Oe, (b) 1198 Oe, (c) 1123 Oe, (d) 1012 Oe, (e) 989 Oe, and (f) 960 Oe. The film thickness is ~2 μm and temperature is 80.5 °C. The edge length of the triangle is 100 μm.

This is shown schematically in Fig. 16(a) along with two examples of bisection rule in Fig. 16(b). Note that once additional domain segments form, determination of trajectory requires additional consideration of magnetostatic forces from those segments. As a result the observed trajectory will be a balance of interactions between all such segments and the approaching domain. Such a deviation is shown in the encircled example in Fig. 16(b), where the actual angle of trajectory is less than the bisector angle owning to forces due to a wall segment on the top. A schematic of such deviation is shown schematically in Fig. 16(c). In such cases, the superposition principle applies by summing over all interactions.

Corollary. Although a new domain may nucleate from an existing domain, from magnetostatic considerations, repulsive forces between flux of same polarity precludes the intersection of one reversed domain with another.

Synthetic Variants. With aforesaid understanding that magnetostatic interactions underpin the observed domain morphology, synthetic patterns can be produced. For example, Movie-7 shows formation of plane-parallel set of reversed domains in a microfabricated square film, with edge length of 200 μm.[35] Initially, a plane-parallel set of reversed

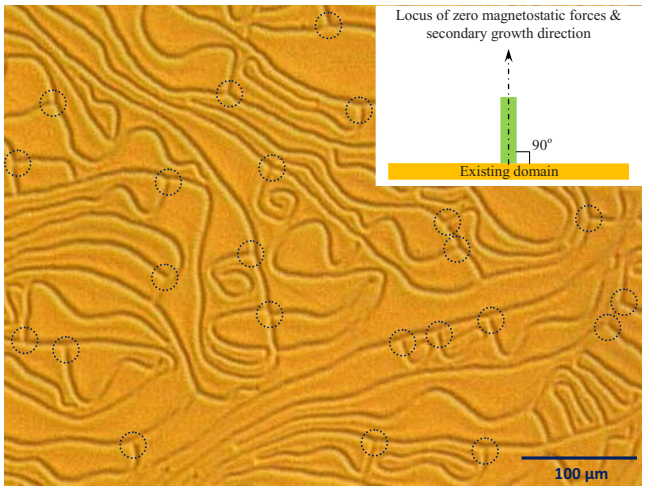

FIG. 15. (Color online) Examples of the orthogonality rule for initial trajectory of a reversed domain along with a schematic of the same in the inset. Numerous orthogonal trajectories of reversed domains at the point of their nucleation are shown encircled and the micrograph is taken from the sequence of images shown earlier in Fig. 4.

domains grows along one of the square diagonals (running from bottom right to top left), as shown in Fig. 17(a). However, the growth along the other square diagonal (running from top right to bottom left) is equally probable. Therefore, once reversed domains branch off orthogonally from existing plane-parallel domains, growth begins to occur along the second diagonal, as shown in Figs. 17(b) and 17(c). The schematic in Fig. 17(d) shows that this gives rise to two variants, whose growth directions are along the two square diagonals.

Fractal dimension. The Euclidian dimension d defines the spatial dimension ($d=1$, 2, and 3 for line, plane, and volume, respectively). The measure of the length, area, or volume is then obtained by discriminating shapes in small elements that have the same Euclidian dimension. However, as mentioned earlier, the recursive nature of the micromagnetic patterns formed by random propagation of self-similar shapes makes the observed micromagnetic structures amenable to characterization using fractal geometry.[39] Fractal nature of magnetic domains and domain walls has previously been studied both experimentally and theoretically.[16–18,36,40–50] In particular, fractal or hierarchical nature of walls has been predicted to dominate magnetostrictive materials based on minimization of energy density.[46] Using a ruler method, it has been shown that the fractal dimension D in Tb-Fe films increases with an increase in temperature up to the Curie point.[40] Using the same method, the fractal dimension was found to decrease with an increase in applied field in Au/Co/Au films with perpendicular anisotropy,[42,44] as well as in Co and Dy-NdFeB single crystals;[18] as shown below, a similar trend (but of different origin) is found in the present study. The process of remagnetization as development of fractal clusters of reversed domains has also been shown.[17] Using Hausdorff-Besicovitch method,[51] fractal nature of phase equilibrium curves has been found in a system of interacting magnetic moments in the presence of a low-

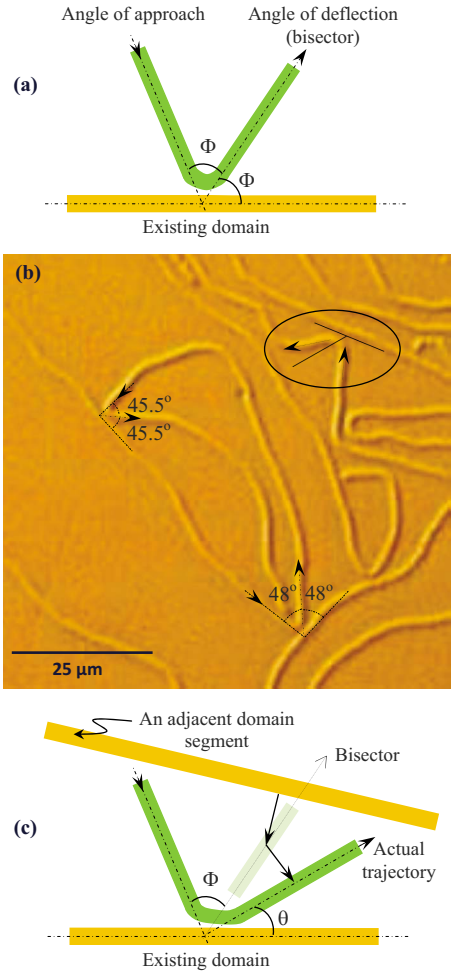

FIG. 16. (Color online) (a) Schematic showing the bisection rule. (b) Two examples of bisection rule where the approaching reversed domain encounters only a single-domain segment. Notice the trajectory of the approaching domains with the aid of the arrows, which shows that the interaction is always between the approaching domain and a single-domain segment. Deviation from bisector angle occurs when the approaching domain encounters more than one domain segment, as shown encircled in (b). In such cases the actual trajectory can be obtained by superposition principle by summing over all interactions. (c) Schematic of such a deviation.

frequency bias field. More recently, a stepwise jump in fractal dimension has been attributed to a phase transition between two types of fractal structures in permalloy films.[49] In order to calculate the fractal dimension D of the observed patterns as a function of applied, field, the operating fractal rule has to take into account the effect of magnetic field as the pattern changes from saturation field to remanence. As shown above, the new reversed domains propagate in such a way that the unreversed domain is continuously subdivided. Therefore fractal geometry occurs by formation of reversed domains at different length scales and such domains can be enumerated. The calculated fractal dimension of the patterns then determines the population of reversed domains as a function of size of unreversed domains and magnetic field. Using the correlation method,[52] the first step was to count the

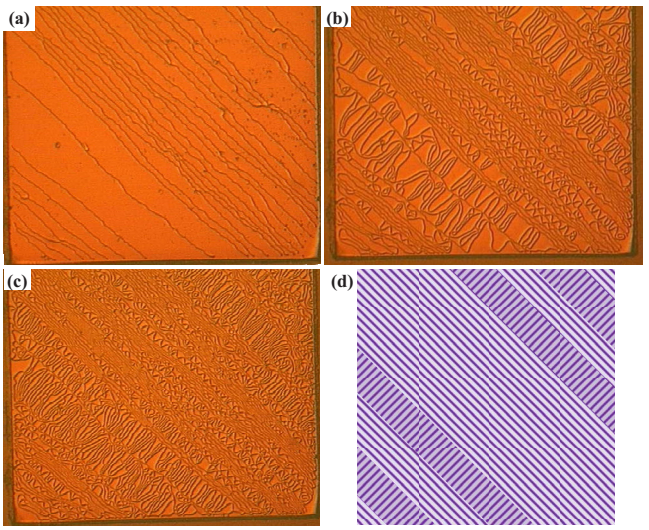

FIG. 17. (Color online) [(a)–(c)] Growth of reversed domains along two square diagonals, giving rise to two variants. The film thickness is ~2 μm and temperature is ~80 °C. Applied fields are (a) 1068 Oe, (b) 957 Oe, and (c) 871 Oe. (d) Schematic of growth pattern, showing directional growth along the two square diagonals.

population of the reversed domains within a box having a size ϵ. Whereas several approaches can be used to calculate the fractal dimension, such as Hausdorff-Besicovitch and Bouligand-Minkowski methods,[51] the correlation method has the advantage of fast computing and has been shown to be equivalent to the fractal law.[52] In this method, a box of size ϵ is first chosen and the population (pixels) of reversed domains within this box is counted. Then the size of the box is increased and the new population counted. The fractal analysis software[53] mathematically fits the increase in population of reversed domains as a function of size of the box using the equation $N(\epsilon)=a\cdot\varepsilon^{D}+c$, where a accounts for the local deviation within the fractal law $[N(\epsilon)=\varepsilon^{D}]$ and c is constant. Note that the general equation relating the population to fractal dimension is $N(\epsilon)=\varepsilon^{D}$. However, the modified equation $[N(\epsilon)=a\cdot\varepsilon^{D}+c]$ is used in practice because real fractals found in nature do not repeat themselves infinitely. Table I shows an example of the variation in various parameters and fractal dimension versus applied field for the film described in Fig. 4. Since fractal dimension D appears as an exponent $[N(\epsilon)=a\cdot\varepsilon^{D}+c]$, the calculated population $N(\epsilon)$ of reversed is closer to the experimental results by keeping D to three decimal points in Table I. For local deviation from the fractal law, the prefactor "a" in Table I is kept to two decimal points to achieve good fit with the experimental results. The constant "c" in Table I is redundant beyond one decimal point. From such data sets, the relationship between populations versus size of the box (size of unreversed domain) can be plotted for different fields, as shown in Fig. 18. For each curve, the ratio between actual population of the pixels and the mathematical fitting of the calculated population is the correlation ratio. The average correlation ratio for all the curves was calculated to be 0.9997; box size less than 15 pixels had too few data points to give consistent results. Figure 19 shows the fractal dimension versus applied field at 100 °C. Although the trend of decreasing fractal dimension

TABLE I. Variation in various parameters of the modified fractal equation and fractal dimension at various applied field values.

Field (Oe)	*a*	*D*	*c*
−1600	0.68	1.630	27.4
−1220	0.46	1.774	35.8
−1045	0.41	1.838	−1.7
−1025	0.43	1.843	−7.4
−1020	0.43	1.847	−8.0
−1010	0.44	1.856	−9.8
−1005	0.53	1.867	−23.6
−1000	0.58	1.869	−28.7
−730	0.72	1.902	−15.5
−500	0.76	1.905	−12.6
−400	0.86	1.906	−14.9
−200	0.76	1.911	−1.7

with increasing field is similar to that observed in Refs. 18, 42, and 44 the underlying origin differs. Notice that the fractal dimension becomes asymptotic to 1.9 at fields lower than 1000 Oe. Initially, at high fields the first set of reversed domains that are formed are really not a fractal as they are not sufficiently subdivided. In other words, there is no self-repeating action during the initial stages. As the magnetic field is decreased, the rate of self-repeating action increases for smaller decreases in applied field, and the subdivision becomes progressively finer. The final structure is the closest approximation of the limiting fractal dimension. The physical meaning of this limiting fractal dimension is that the reversed domains ultimately cover the entire area such in such a manner that the net magnetization is close to the remanence. As mentioned earlier, knee a represents the first time-reversed domains are formed, and they may be considered to be the *initiators* of the subsequent self-similar process. Between knees a and b, the structure is still too coarse to be characterized as a fractal. Below knee b, the subdivision becomes finer and that is when one starts to get a more consistent fractal dimension. Optical micrographs close to knee c do not have enough resolution to be investigated. Finally, given that thermal-expansion coefficient of Tb-Fe is greater than that for silicon substrate,[28–30] a higher temperature results in greater compressive thermal stress in the film (due to thermal-expansion coefficient mismatch) and a higher perpendicular anisotropy. Higher domain-wall energy is associated with higher anisotropy. At the same time, a lower magnetization length (saturation magnetization) at higher temperature gives weaker magnetostatic interaction. Due to decreased magnetostatic interaction and higher domain-wall energy at higher temperature, the domain size is increased (coarser domain). Related micromagnetic simulations are currently underway and will be reported in a future publication.[54] Also, it has been previously shown that the equilibrium width of stripe domains is defined by film parameters[12] and is on the order of the sample thickness.[14] Therefore it is of interest to note that in the present study, the width of the domains varies as the self-similar domain reversal progresses, see, for example, Figs. 4 and 7. Theoretical and experimental work is currently underway to model this observed behavior and will be reported in a later publication.[54]

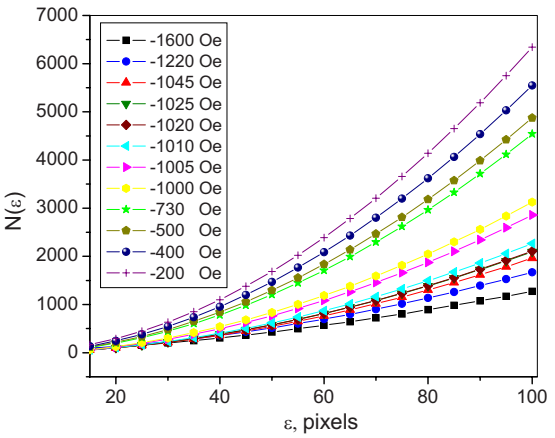

FIG. 18. (Color online) The relationship between populations $N(\epsilon)$ versus size of the box ϵ.

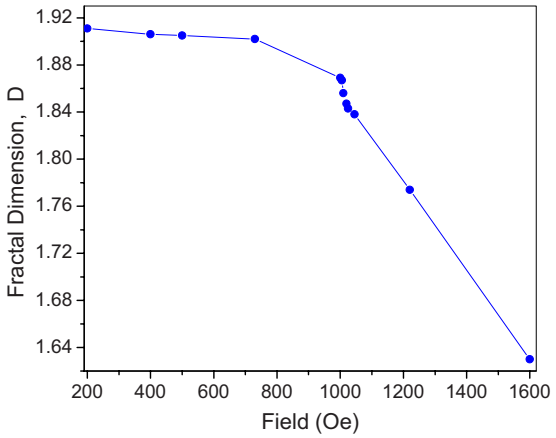

FIG. 19. (Color online) Fractal dimension versus applied field at 100 °C.

IV. CONCLUSIONS

The apparently complex maze-like domain patterns in amorphous medium with perpendicular anisotropy are shown to be simple, being composed of the same geometrical forms that gradually fill in the unreversed regions at progressively smaller scales to minimize the magnetostatic energy. The self-similar growth morphogenesis of domains is fractally enumerated.

Geometrical rule-1. Balanced by magnetostatic forces, the initial trajectory of a nucleating reversed domain as a branch of an existing domain is orthogonal to the existing domain.

Geometrical rule-2. The locus of any Maiandros (open or closed) in its approach to another segment of reversed domain is the bisector of the angle between the two. For cases involving more than two domain segments, the superposition principle applies by summing over all interactions.

Although a new domain may nucleate from an existing domain, from magnetostatic considerations, repulsive forces

between flux of same polarity precludes the intersection of one reversed domain with another.

The initial kink in the hysteresis curve close to saturation fields corresponds to the appearance of the first set of reversed domains that subdivide a single unreversed domain into a multiplicity of unreversed domains. Subsequent reversal process in any unreversed region occur independent of reversal in adjacent regions.

Finally, results provide an example where microscopic changes (self-similar morphogenesis of domains) are signaled by a distinct signature in the measured macroscopic property (knees in the hysteresis curves), instead of being smeared out in the average macroscopic property.

ACKNOWLEDGMENTS

This work was supported by the National Science Foundation, Grants No. DMR-0706074 and No. DMR-0305242, and this support is gratefully acknowledged. The authors acknowledge E. Quandt and A. Ludwig for one of the films used in the present study. H.D.C. also acknowledges useful discussions with Yongmei Jin at Michigan Tech.

*Corresponding author; hchopra@buffalo.edu

[1] M. R. Sullivan and H. D. Chopra, Phys. Rev. B **70**, 094427 (2004).
[2] M. R. Sullivan, S. J. Pirotta, V. A. Chernenko, G. H. Wu, G. Balasubramanium, S. Z. Hua, and H. D. Chopra, Int. J. Appl. Electromagn. Mech. **22**, 11 (2005).
[3] J. N. Armstrong, M. R. Sullivan, and H. D. Chopra, Phys. Rev. B **80**, 104429 (2009).
[4] Q. Su, Y. Zheng, A. Roytburd, and M. Wuttig, Appl. Phys. Lett. **66**, 2424 (1995).
[5] T. G. Pokhil, J. Appl. Phys. **81**, 5035 (1997).
[6] J. Miguel, J. F. Peters, O. M. Toulemonde, S. S. Dhesi, N. B. Brookes, and J. B. Goedkoop, Phys. Rev. B **74**, 094437 (2006).
[7] F. Hellman, A. L. Shapiro, E. N. Abarra, R. A. Robinson, R. P. Hjelm, P. A. Seeger, J. J. Rhyne, and J. I. Suzuki, Phys. Rev. B **59**, 11408 (1999).
[8] P. J. Grundy, E. T. M. Lacey, and C. D. Wright, J. Magn. Magn. Mater. **54-57**, 227 (1986).
[9] J. N. Armstrong, M. R. Sullivan, M. Le Romancer, V. A. Chernenko, and H. D. Chopra, J. Appl. Phys. **103**, 023905 (2008).
[10] C. Kooy and U. Enz, Philips Res. Rep. **15**, 7 (1960).
[11] K. De'Bell, A. B. MacIsaac, and J. P. Whitehead, Rev. Mod. Phys. **72**, 225 (2000).
[12] A. Kashuba and V. L. Pokrovsky, Phys. Rev. Lett. **70**, 3155 (1993).
[13] O. Portmann, A. Vaterlaus, and D. Pescia, Nature (London) **422**, 701 (2003).
[14] V. Gehanno, A. Marty, B. Gilles, and Y. Samson, Phys. Rev. B **55**, 12552 (1997).
[15] S. Konings, J. Miguel, J. Luigjes, H. Schlatter, H. Luigjes, J. Goedkoop, and V. Gadgil, J. Appl. Phys. **98**, 054306 (2005).
[16] F. V. Lisovskiĭ, E. G. Mansvetova, and C. M. Pak, JETP Lett. **60**, 136 (1994).
[17] L. Dovbnya, D. Naumov, and B. Khramov, JETP Lett. **73**, 366 (2001).
[18] B.-S. Han, D. Li, D.-J. Zheng, and Y. Zhou, Phys. Rev. B **66**, 014433 (2002).
[19] A. P. Malozemoff and J. C. Slonczewski, *Applied Solid State Science Supplement 1: Magnetic Domain Walls in Bubble Materials* (Academic Press, New York, 1979).
[20] M. Seul and D. Andelman, Science **267**, 476 (1995).
[21] T. Katayama, M. Hirano, Y. Koizumi, K. Kawanishi, and T. Tsushima, IEEE Trans. Magn. **13**, 1603 (1977).
[22] H. Takagi, S. Tsunashima, S. Uchiyama, and T. Fujii, J. Appl. Phys. **50**, 1642 (1979).
[23] H. Takagi, S. Tsunashima, S. Uchiyama, and T. Fujii, Jpn. J. Appl. Phys. **18**, 399 (1979).
[24] S. Yoshino, H. Takagi, S. Tsunashima, M. Masuda, and S. Uchiyama, Jpn. J. Appl. Phys., Part 1 **23**, 188 (1984).
[25] S. N. Cheng, M. H. Kryder, and M. C. A. Mathur, IEEE Trans. Magn. **25**, 4018 (1989).
[26] P. Hansen, J. Appl. Phys. **62**, 216 (1987).
[27] S.-C. N. Cheng and M. H. Kryder, J. Appl. Phys. **70**, 5526 (1991).
[28] S. M. Na, S. J. Suh, and S. H. Lim, J. Appl. Phys. **93**, 8507 (2003).
[29] F. Schatz, M. Hirscher, M. Schnell, G. Flik, and H. Kronmuller, J. Appl. Phys. **76**, 5380 (1994).
[30] K. Yamada, A. Fujita, M. Ohta, and K. Fukamichi, J. Magn. Magn. Mater. **239**, 412 (2002).
[31] U. Hartmann and H. H. Mende, J. Phys. D: Appl. Phys. **18**, 2285 (1985).
[32] F. Bitter, Phys. Rev. **38**, 1903 (1931).
[33] H. D. Chopra, M. R. Sullivan, A. Ludwig, and E. Quandt, Phys. Rev. B **72**, 054415 (2005).
[34] M. R. Sullivan, A. A. Shah, and H. D. Chopra, Phys. Rev. B **70**, 094428 (2004).
[35] See supplementary material at http://link.aps.org/supplemental/10.1103/PhysRevB.82.184411 for documents including Movie-1 showing evolution of domain structure versus field in a 2.2-μm-thick amorphous Tb-Fe film at ~100 °C as the field is reduced from negative saturation to zero. Movie-1 corresponds to micrographs shown in Fig. 4. Movie-2 shows evolution of domain structure versus field in a 2.2-μm-thick amorphous Tb-Fe film at ~100 °C as the field is increased from zero to negative saturation. Movie-2 corresponds to micrographs shown in Fig. 7. Movie-3 shows recursive size reduction at different length scales in a 2-μm-thick amorphous Tb-Fe film at 93 °C, Movie-3 corresponds to the sample shown in Fig. 1(d). Movie-4 shows progressive morphogenesis of reversed domains into a near-perfect plane-parallel assembly. Movie-4 corresponds to micrographs shown in Fig. 12. The edge length of the triangle is 150 μm. The film thickness is ~2.3 μm and temperature is 54.5 °C. Movie-5 shows progressive morphogenesis of reversed domains into an imperfect assembly of plane-parallel domains. Movie-5 corresponds to micrographs shown in Fig. 13. The edge length of the triangle is 100 μm. The film thickness is ~2 μm

and temperature is 80.5 °C. Movie-6 shows progressive morphogenesis of reversed domains into a random assembly of plane-parallel domains. Movie-6 corresponds to micrographs shown in Fig. 14. The edge length of the triangle is 100 μm. The film thickness is ~2 μm and temperature is 80.5 °C. Movie-7 shows formation of plane-parallel set of reversed domains in a microfabricated square film with edge length of 200 μm. Movie-7 corresponds to micrographs shown in Fig. 17. The film thickness is ~2 μm and temperature is ~80 °C. In all movies, the applied field is normal to the plane of the screen.

[36] J. P. Attané, Y. Samson, A. Marty, J. C. Toussaint, G. Dubois, A. Mougin, and J. P. Jamet, Phys. Rev. Lett. **93**, 257203 (2004).
[37] C. Kittel, Rev. Mod. Phys. **21**, 541 (1949).
[38] C. Strauss, Nature (London) **446**, 725 (2007).
[39] B. B. Mendelbrot, *Fractals: Form, Chance, and Dimension* (W. H. Freeman, San Francisco, 1977).
[40] B. E. Bernacki and M. Mansuripur, J. Appl. Phys. **69**, 4960 (1991).
[41] G. V. Sayko, A. K. Zvezdin, T. G. Pokhil, B. S. Vvedensky, and E. N. Nikolaev, IEEE Trans. Magn. **28**, 2931 (1992).
[42] A. Kirilyuk, J. Ferré, and D. Renard, Europhys. Lett. **24**, 403 (1993).
[43] A. Lyberatos, J. Earl, and R. W. Chantrell, Phys. Rev. B **53**, 5493 (1996).
[44] A. Kirilyuk, J. Ferré, V. Grolier, J. P. Jamet, and D. Renard, J. Magn. Magn. Mater. **171**, 45 (1997).
[45] F. V. Lisovskiĭ and O. P. Polyakov, JETP Lett. **68**, 679 (1998).
[46] R. Blumenfeld, Phase Transitions **69**, 237 (1999).
[47] D.-H. Kim, Y.-C. Cho, S.-B. Choe, and S.-C. Shin, Phys. Status Solidi B **241**, 1669 (2004).
[48] D. Aurongzeb, Appl. Phys. Lett. **89**, 123128 (2006).
[49] F. V. Lisovskiĭ, L. Lukashenko, and E. Mansvetova, JETP Lett. **79**, 352 (2004).
[50] G. Catalan, H. Béa, S. Fusil, M. Bibes, P. Paruch, A. Barthélémy, and J. F. Scott, Phys. Rev. Lett. **100**, 027602 (2008).
[51] J. F. Gouyet, *Physics and Fractals Structures* (Springer-Verlag, New York, 1996).
[52] P. Grassberger and I. Procaccia, Physica D **9**, 189 (1983).
[53] P. Frankhauser and C. Tannier, CNRS-Université de Bourgogne et de France-Comté, software developed by Gilles Vuidel, 2006.
[54] Y. Jin and H. D. Chopra (unpublished).